J Comput Electron
DOI 10.1007/s10825-012-0403-1

A multi scale modeling approach to non-radiative multi phonon transitions at oxide defects in MOS structures

F. Schanovsky · O. Baumgartner · V. Sverdlov · T. Grasser

Abstract We discuss a novel approach to predict non-radiative multi phonon (NMP) transition rates for oxide defects in semiconductor devices in the context of device reliability. In accordance with NMP theory, the influence of the atomic vibration on the electronic transition is assumed to be fully described by the line shape function. This line shape is calculated from density functional theory for a given defect structure and then combined with the carrier spectrum from a non-equilibrium Green's function model of the semiconductor device. Hole capture rates at different temperatures and bias conditions are computed for two well-studied defect structures, the oxygen vacancy and the hydrogen bridge, at different positions in the oxide of an MOS structure.

Keywords Bias temperature instabilities · BTI · Random telegraph noise · RTN · Non-radiative multi phonon theory · NMP · Temperature activated hole capture · Density functional theory · DFT · Multi scale modeling

1 Introduction

Carrier trapping at defects in insulating oxide layers gives rise to many reliability issues in semiconductor devices such as the bias temperature instability (BTI) [1–4], random telegraph noise (RTN) and flicker ($1/f$) noise [5–9], and stress-induced leakage currents [10, 11]. The empirically observed kinetics in all of these effects show a strong temperature activation, which is usually attributed to the influence of the atomic motion of the defect structure on the charge transition. Also, a structural relaxation of the defect is required to follow the charge transitions to explain some of the observed behavior [5, 6]. The physical foundation of the charge transitions involved in these effects lies in the theory of non-radiative multi phonon (NMP) transitions [12, 13].

NMP theory has been used by several authors in the context of semiconductor devices [6, 14–17] to explain the observed energy dependent capture cross sections [18, 19]. The transition rate formulas employed are usually based on linear electron-phonon coupling. Further, it is either assumed that the transition couples to an infinite number of phonon modes—all having the same oscillator strength—where each can contribute only one phonon [12, 16, 17], or that the transition couples to only one mode which receives or emits an arbitrary number of phonons [13, 14]. Interestingly, for linear coupling modes both assumptions lead to essentially the same expression for the capture rates. The model parameters are usually determined by calibration to measurement data. Especially for the modeling of BTI and RTN, however, this method is somewhat unsatisfactory as the measurements show a broad spread in transition rates [8] and the occurrence of structural reorganization of the defects [5, 20]. This requires a large set of statistically distributed parameters that have to be obtained by fitting the model to experimental data. In order to obtain a clear understanding of the meaning of these parameters it would be favorable to interpret the experimental data in terms of a concrete atomistic defect model instead of an abstract parameter set.

The present work reports on a multi-scale modeling approach to the problem, combining state-of-the-art device modeling with a first-principles density functional theory (DFT) based description of the defect properties. It is meant as a proof-of-concept for extracting NMP parameters for device modeling from DFT and also serves as a benchmark for

F. Schanovsky (✉) · O. Baumgartner · V. Sverdlov · T. Grasser
Institute for Microelectronics, TU Wien, Gußhausstraße 27-29/E360, 1040 Wien, Austria
e-mail: schanovsky@iue.tuwien.ac.at

Published online: 30 May 2012

computationally less expensive approximations. This work builds on our previous investigations of the vibrational coupling in hole capture transitions at oxide defects [21–23] and is an extended presentation of [24]. It closes the gap between atomic level calculations and semiconductor device modeling by directly employing DFT calculated line-shape functions in an open boundary quantum mechanical device simulation.

Relating this description to the two versions of vibronic coupling mentioned before, we assume that the NMP kinetics are determined by a small number of local modes at the defect site. A coupling to a large number of modes does not seem reasonable for the defects involved in BTI and RTN considering the large variations in transition rates between the defects that are observed in measurements. These variations can only be explained by differences in the local environment of the defect structure which can only hold a small number of vibrational modes.

As examples we apply the method to hole capture at oxide defects in an MOS structure. The model defect structures studied are the hydrogen bridge and the (puckered) oxygen vacancy in α-quartz, which are both well-studied defect structures [11]. The predicted capture rates are compared to time dependent defect spectroscopy (TDDS) [6, 20] measurements on small-area pMOSFETs. In these measurements, a large negative bias pulse is applied to the gate of the transistor, while the other terminals are grounded. Afterwards, the drain current is monitored and usually mapped to a threshold voltage shift ΔV_{th}. This set-up resembles NBTI measurements of large-scale devices, where the bias pulse is called stress and the following monitoring phase is called recovery. However, contrary to the continuous recovery transients observed in large-scale devices, the threshold voltage shift changes in discrete steps, as illustrated in Fig. 1. These steps have been attributed to discharging of oxide defects that have captured a hole during the stress phase. Careful analysis of a large set of recovery traces makes it possible to extract the average capture and emission time constants of individual defects. It is then possible to study the dependence of these time constants on V_{G} as in Fig. 7.

2 NMP transitions

Charge transition processes involving multiple vibrational excitations of defects in semiconductors have been extensively studied in literature [12–14, 17, 25]. The rate k_{if} for an NMP transition from the initial electronic state $|\Phi_{\mathrm{i}}\rangle$ to the final electronic state $|\Phi_{\mathrm{f}}\rangle$ is given by

$$k_{\mathrm{if}} = A_{\mathrm{if}} f, \tag{1}$$

where A_{if} describes the electronic part of the transition and f is the so-called line shape function, which describes the vibrational influence.

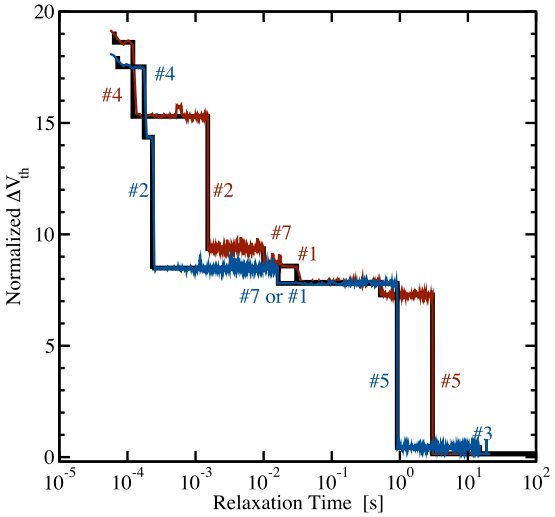

Fig. 1 In small-area pMOSFETs, NBTI recovery traces feature steps of varying size at different relaxation times. These steps have been attributed to the stochastic discharging of defects that have captured a hole during the stress phase. Using the TDDS method, the capture and emission kinetics of these defects can be studied [6]

2.1 Electronic matrix element

The first factor in Eq. (1),

$$A_{\mathrm{if}} = \frac{2\pi}{\hbar} \left|\langle \Phi_{\mathrm{f}} | V' | \Phi_{\mathrm{i}} \rangle\right|^2, \tag{2}$$

contains the electronic matrix element between the initial and the final electronic state $|\Phi_{\mathrm{i}}\rangle$ and $|\Phi_{\mathrm{f}}\rangle$ via the perturbing potential V'. In a semiconductor device, none of these quantities is accurately known, and so this term has to be estimated [3, 14, 15]. In the present work, we approximate it as [22]

$$\left|\langle \Phi_{\mathrm{f}} | V' | \Phi_{\mathrm{i}} \rangle\right|^2 \approx \alpha \left|\langle x_{\mathrm{d}} | \phi_j \rangle\right|^2, \tag{3}$$

where x_{d} is the position of the defect and $|\phi_j\rangle$ is the free-carrier wave function. This reduces the electronic matrix element to a tunneling expression and adds a prefactor that accounts for the physics neglected in the approximation. The tunneling of carriers to the defect position is usually calculated using a Wentzel-Kramers-Brillouin (WKB) expression on top of a classical device simulation [3]. Quantum-mechanical device simulation has also been used in [15] and the present work. The consequence of approximation Eq. (3) is that all capture rates calculated in the present work are accurate to a constant factor, therefore all computed time constants in Sect. 5 are given in arbitrary units.

2.2 Line shape function

The second factor in Eq. (1),

$$f = \operatorname*{ave}_{\alpha} \sum_{\beta} \left|\langle \eta_{\mathrm{f}\beta} | \eta_{\mathrm{i}\alpha} \rangle\right|^2 \delta(E_{\mathrm{f}\beta} - E_{\mathrm{i}\alpha} \pm E), \tag{4}$$

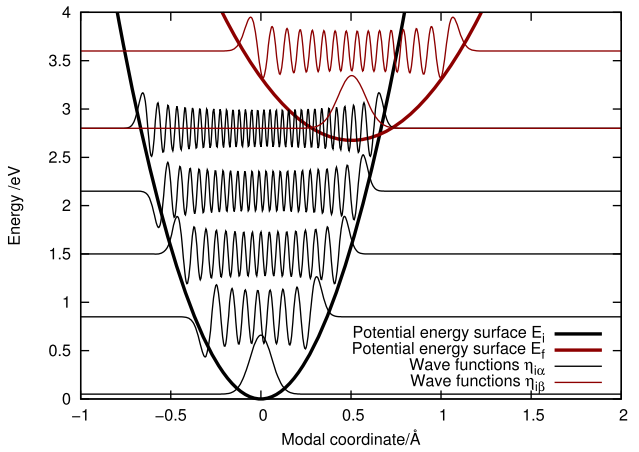

Fig. 2 Different electronic states $|\Phi_\mathrm{i}\rangle$ and $|\Phi_\mathrm{f}\rangle$ give rise to different potential energy surfaces E_i and E_f for the atoms. A change in the electronic state of a defect changes the corresponding potential energy surface and in consequence the vibrational wave functions. To compute the rate of the transition $|\Phi_\mathrm{i}\rangle \rightarrow |\Phi_\mathrm{f}\rangle$, the overlaps between all initial and final vibrational states have to be taken into account

is called the line shape function. It describes the dependence of the capture rate on the carrier energy E and is an inherent property of the atomic structure of the defect. The line shape is determined by the overlaps of the vibrational wave functions $|\eta_{\mathrm{i}\alpha}\rangle$ and $|\eta_{\mathrm{f}\beta}\rangle$ associated with the initial and the final adiabatic potential energy surface E_i and E_f as well as the respective energies $E_{\mathrm{f}\beta}$ and $E_{\mathrm{i}\alpha}$, see Fig. 2. The carrier energy E is the energy of the reservoir state that is involved in the transition. It is added for hole capture (electron emission), and subtracted for electron capture (hole emission).

2.2.1 *Line shapes from DFT*

We have recently devised a method to extract the line shape function from DFT defect calculations [21, 23]. In this method, approximate potential energy surfaces are extracted from DFT calculations as depicted in Fig. 3. These parabolic potential energy surfaces define harmonic oscillator vibrational wave functions for the defect in the initial and the final charge state. Finally, the overlap integrals of the harmonic oscillator wave functions, for which analytic expressions exist [26, 27], are used to construct line shapes via Eq. (4). The resulting line shapes consist of weighted Dirac peaks. These peaks are artifacts of the single-mode description and the neglect of the energetic contribution of the perturbation operator. The result is corrected to give continuous line shapes by smearing with a normal distribution of standard deviation $k_\mathrm{B}T$. A more in-depth description of the line shape calculation can be found in [23], the results for the defects under consideration can be seen in Fig. 3. Especially the potentials extracted from the puckered oxygen vacancy (Fig. 3 right) show clearly that the usually assumed linear electron-phonon coupling [15–17], which leaves the vibrational frequency unchanged, is not applicable here.

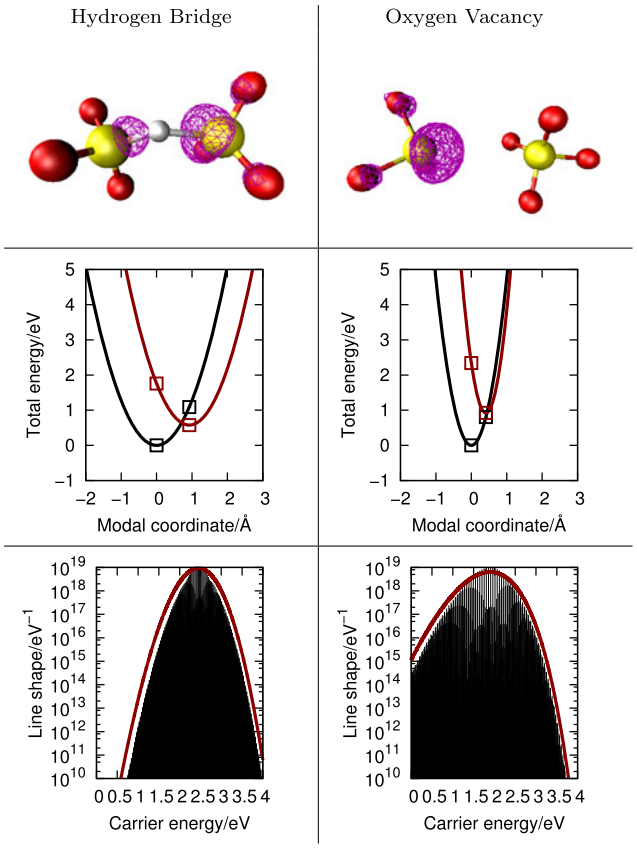

Fig. 3 Results from our DFT calculations for the hydrogen bridge (*left*) and the oxygen vacancy (*right*). (*top*) The structures employed in our calculations, reduced to the atoms immediately surrounding the defect. The partial charge densities associated with the defect are shown as wire frame. (*center*) To extract line shapes from DFT calculations, approximate parabolic potential energy surfaces are extracted for the defect in its neutral (*black*) and positive (*red*) state. The *square symbols* indicate the points calculated using DFT [21]. (*bottom*) The extracted line shape functions at 300 K. The weighted Dirac peaks from Eq. (4) are indicated in *black*, the *red curves* show the smeared results (Color figure online)

2.2.2 *Classical line shapes*

When quantum effects in the atomic motion can be neglected, the line shapes become simple analytic expressions which can be easily implemented into a device simulator. In the classical case, the electronic transition happens exactly at the crossing points of the potential energy surfaces [28]. The line shape Eq. (4) is calculated as

$$f(E) = Z^{-1} \int_q \mathrm{e}^{-E_\mathrm{i}(q')/k_\mathrm{B}T} \delta\big(E_\mathrm{f}(q') - E_\mathrm{i}(q') + E\big)\mathrm{d}q', \tag{5}$$

with the partition function

$$Z = \int_q \mathrm{e}^{-E_\mathrm{i}(q')/k_\mathrm{B}T}\mathrm{d}q'. \tag{6}$$

For the harmonic potentials $E_\mathrm{i}(q) = c_\mathrm{i}q^2$ and $E_\mathrm{f}(q) = c_\mathrm{f}(q - q_\mathrm{s})^2 + E_\mathrm{s}$, where the parameters q_s, c_i, c_f, and E_s

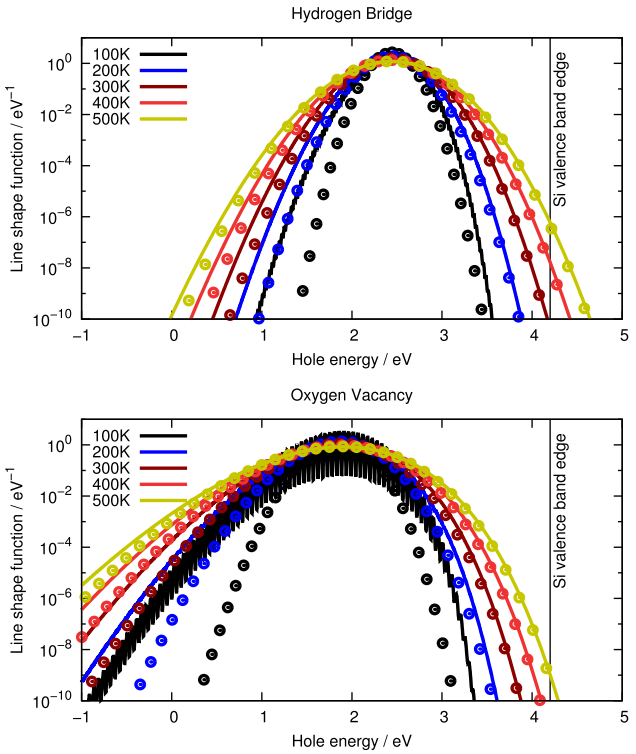

Fig. 4 Comparison of the classical line shapes from Eq. (7) (*symbols*) to their quantum mechanical counterpart that was calculated numerically from Eq. (4) (*lines*) at the indicated temperatures. The 100 K plots show oscillations as the quantum mechanical nature of the vibrational overlaps becomes more and more pronounced in this regime. Deviations between the two formulas arise at low temperatures and in the weak coupling regime (energies below the peak of the line shape) due to the absence of tunneling in the classical version

are extracted from DFT, the classical line shape reads

$$f(E) = \frac{\sqrt{k_\mathrm{B} T k_\mathrm{i} \pi^{-1}}}{2} \times \left(\frac{\mathrm{e}^{-c_\mathrm{i} q_1^2 / k_\mathrm{B} T}}{|c_\mathrm{i} q_1 + c_\mathrm{f}(q_\mathrm{s} - q_1)|} + \frac{\mathrm{e}^{-c_\mathrm{i} q_2^2 / k_\mathrm{B} T}}{|c_\mathrm{i} q_2 + c_\mathrm{f}(q_\mathrm{s} - q_2)|} \right), \tag{7}$$

where

$$q_{1,2} = \frac{c_\mathrm{f} q_\mathrm{s} \pm \sqrt{c_\mathrm{i} c_\mathrm{f} q_\mathrm{s}^2 + (c_\mathrm{i} - c_\mathrm{f})(E + E_\mathrm{s})}}{c_\mathrm{f} - c_\mathrm{i}}. \tag{8}$$

The quantum mechanically calculated line shapes are compared to their classical counterpart in Fig. 4. It shows that the classical formula underestimates the transition rate at low temperatures and for energies that are below the maximum of the line shape, which correspond to the weak coupling regime of the defect [29]. These underestimations are due to the neglect of tunneling in the classical model. For strong coupling, which is especially relevant for the exchange of holes with the silicon valence band, good agreement between the classical and the quantum mechanical version is already given at room temperature.

2.3 Total capture rate

The rate k_if in Eq. (1) is the rate for the transition between *one* free carrier state $|\phi_j\rangle$ and the localized defect state. In a semiconductor device, there is a *reservoir* of free carriers with different energies E_j, wave functions $|\phi_j\rangle$, associated occupation probabilities p_j, and multiplicities m_j. All of these reservoir states separately contribute a possible reaction path. Using Eq. (3), the total capture rate k_tot is found by summing up the contributions of all particles in the reservoir as

$$k_\mathrm{tot} = \sum_\mathrm{i} k_\mathrm{if} = \alpha \sum_j p_j m_j \left| \langle x_\mathrm{d} | \phi_j \rangle \right|^2 f(E_j) \tag{9}$$

for capture while for emission we have

$$k_\mathrm{tot} = \alpha \sum_j (1 - p_j) m_j \left| \langle x_\mathrm{d} | \phi_j \rangle \right|^2 f(E_j). \tag{10}$$

3 Non-equilibrium Green's functions

In the present work, the carrier concentration of the MOS structure has been calculated self-consistently using a non-equilibrium Green's function (NEGF) method [30]. One advantage of the NEGF approach is the absence of any artificial boundaries within the device, e.g. a Dirichlet boundary condition at the semiconductor-oxide-interface as usually employed in closed-boundary MOS device calculations [15, 16]. Also, it allows the injection of carriers from the gate to be taken into consideration.

The formalism assumes thermal equilibrium in the gate and bulk region where level broadening due to scattering is modeled using an optical potential [30]. The oxide is treated as a non-equilibrium domain with ballistic quantum transport.

3.1 NEGF and line shapes

Due to the open boundary conditions, there are no discrete eigenstates for the hole wave functions. Instead, there is a nonzero probability to find a hole at every energy level. From the Green's function, the local density of states

$$D(x, E) = m(E) \left| \langle x | \phi(E) \rangle \right|^2 \delta(E) \tag{11}$$

as well as the occupation probability $p(x, E)$ can be computed. To obtain the total NMP hole capture rate k_tot for a defect at position x_d, one just has to insert these quantities into Eq. (9) and replace the sum by an integral to obtain

$$k_\mathrm{tot} = \alpha \int f(E) h(x_\mathrm{d}, E) \mathrm{d}E \tag{12}$$

with the hole density

$$h(x, E) = p(x, E) D(x, E). \tag{13}$$

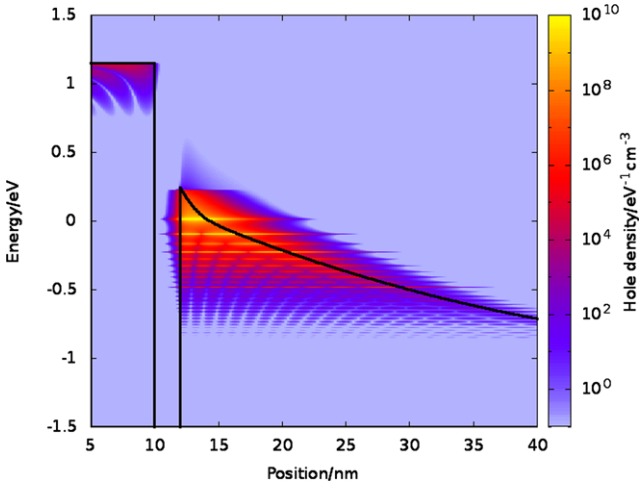

Fig. 5 The spatially and energetically distributed hole density as calculated using the NEGF method. Thermal equilibrium in the gate and the silicon bulk is induced via an optical potential. The penetration of holes into the oxide can be clearly seen

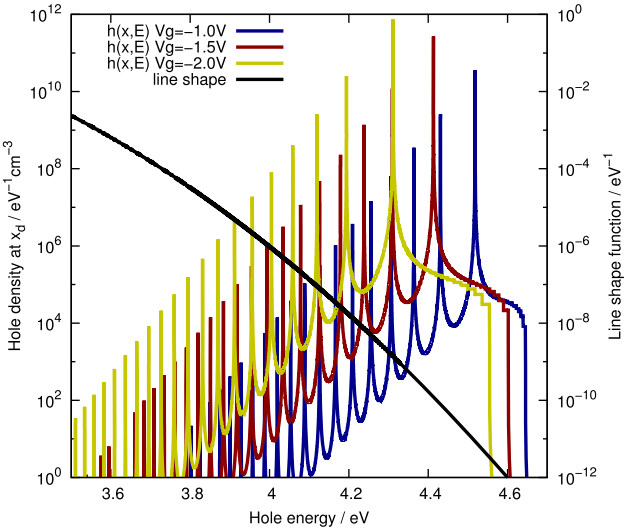

Fig. 6 Illustration of the bias induced shift of the relative position of the line shape and the free-hole states. A hydrogen bridge line shape is used, the defect position is 2 Å from the Si/SiO_2 interface. With more negative gate voltage, the overlap between $f(E - E_v(x_d))$ and $h(x_d, E)$, and in consequence the transition rate, strongly increases

An example hole density as calculated from NEGF is shown in Fig. 5. The integration is implemented as a post-processing step using the numerical NEGF and line shape data.

3.2 Band bending

Especially for oxide defects, where due to the absence of native carriers the application of a gate voltage induces the largest electric field and in consequence the largest band bending, it is necessary to maintain a clear energetic reference for the line shape functions. The energetic shift between the potential energy surfaces of the defect in its different charge states (see Fig. 2 and Fig. 3) depends on the energy of the reservoir state involved. A band bending shifts the relative position of the defect energies and the reservoir energies [21], that has to be accounted for in the calculation of the transition rates. For the evaluation of the integral Eq. (12), we chose the SiO_2 valence band edge E_v, which was also taken as the reference energy in the DFT calculations, as the common alignment energy. The capture rate (12) equation thus changes to

$$k_{tot} = \alpha \int f\big(E - E_v(x_d)\big) h(x_d, E) dE. \tag{14}$$

As illustrated in Fig. 6, the dependence of the line shape on the value of the reference energy at the defect site plays a crucial role for the transition kinetics, as the band bending energetically shifts the relative position of the line shape and the spectrum of the hole states, leading to large changes in the capture rate.

4 Calculation details

The electronic structure of the defect is described with DFT using the PBE functional [31, 32]. The atomistic host lattice is an orthorhombic alpha-quartz supercell structure [11, 21] containing 72 atoms. Alpha-quartz was chosen because it is a well studied reference system for amorphous silica [11, 33, 34]. The defect energies are aligned to the hole reservoir using the valence level of the DFT reference system [35], as the energy levels of the investigated defects are in the lower half of the SiO_2 band gap. More details on the DFT part can be found elsewhere [21–23].

The MOS device is described using the Vienna Schrödinger-Poisson software package (VSP2) [36]. It consists of a poly-Si gate and an n-doped bulk separated by a 2 nm SiO_2 layer. For electrons the unprimed and primed valleys with 0.19 m_e and 0.91 m_e electron mass are included. Holes were considered with 0.49m_e effective mass.

The calculation of the NMP hole capture rates proceeds in a two-step process. First, the band bending is calculated by solving the Poisson- and the NEGF equations self-consistently. Secondly, the NEGF problem is again solved non-self-consistently on a different energy grid that accounts for high-energy holes as these contribute considerably to the NMP transitions.

5 Results

Figure 7 left shows the gate voltage dependence of the NMP hole capture time constants for the two model de-

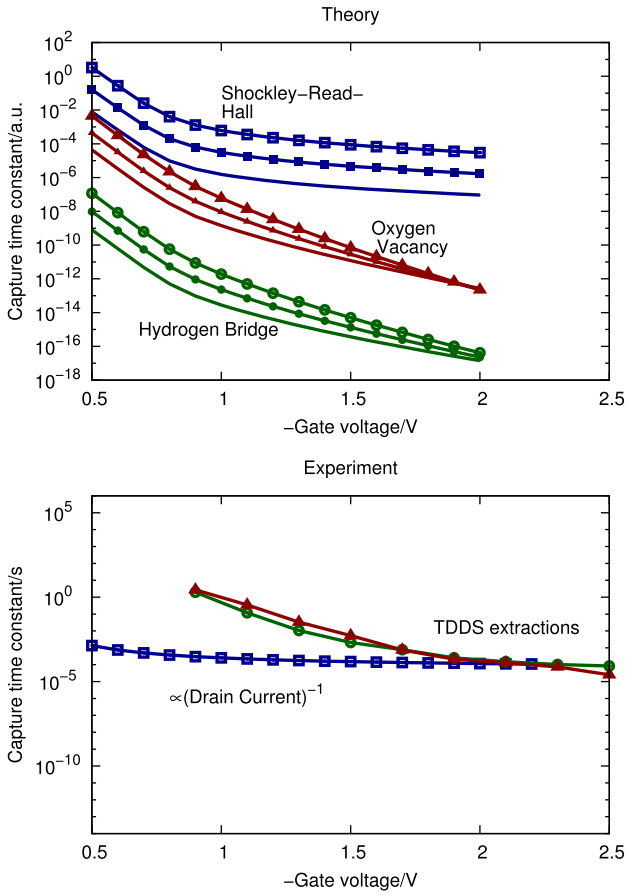

Fig. 7 Gate voltage dependence of the hole capture time constant. The calculated time constants are in arbitrary units, as explained in Sect. 2.1. In the *top figure*, the results for the hydrogen bridge and for the oxygen vacancy are compared to a Shockley-Read-Hall-like capture model, which shows much weaker gate voltage dependence in deep inversion. The calculation temperature is 400 K and the defect position is 2 (*no symbols*), 4 (*medium sized symbols*) and 6 (*large symbols*) angstroms from the silicon bulk. The *bottom figure* shows the experimental situation. Capture time constants extracted using the TDDS technique [6] are compared with the inverse of the drain current, which is proportional to what would be seen for Shockley-Read-Hall-like defects

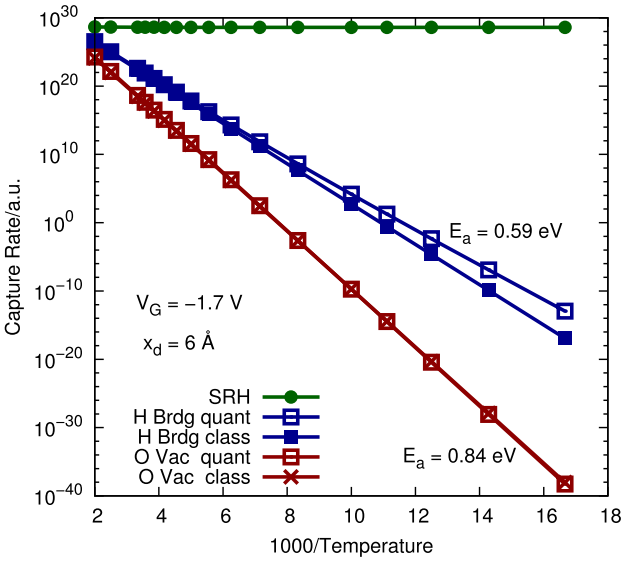

Fig. 8 Arrhenius plots of the capture rates for the defect types comparing the quantum mechanical NMP capture rates Eq. (4) for the oxygen vacancy and the hydrogen bridge to the capture rates calculated using classical atoms Eq. (7) and to a Shockley-Read-Hall like model

fects. The NMP time constants are compared to time constants typically employed in semiconductor device simulation, where the concentration of carriers at the defect site is multiplied with a field and temperature *independent* capture cross section $\tau = \sigma h(x)$. We follow the usual practice to refer to the latter variant as the standard Shockley-Read-Hall (SRH) [37] description. It is important to stress that in this work we are only concerned with the calculation of *capture* rates. The calculation of emission rates in a simple case can proceed using the statistical arguments of Shockley et al. [37] as has been done by several authors [13–15, 25, 38]. The NMP defects clearly show a much stronger gate voltage dependence than the SRH defect. Further, the gate voltage dependence increases with the distance of the defect from the silicon bulk. Both of these strong dependencies are caused primarily by the energetic shift of the line shape functions relative to the holes in the inversion layer as illustrated in Fig. 6. Comparing the bottom part in Fig. 7 shows that the NMP defects are consistent with the qualitative behavior of defects observed in TDDS measurements. The voltage dependence of the TDDS extracted capture time constants also clearly exceeds the voltage dependence of a trapping model with constant capture cross section. In the linear regime of the transistor, the capture rate of such a process would be approximately proportional to the drain current.

The temperature dependence of the hole capture is shown in Fig. 8. The calculation of NMP hole capture rates for the given defects becomes technically challenging for low temperatures. As the temperature decreases, the line shapes become increasingly narrow, thus making high-energy holes the dominantly captured particles. Accurate representation of high-energy holes in the NEGF algorithm requires an improved refinement strategy for the energy grid. To overcome this limitation, the hole distribution over energy was calculated from a classical density of states for the Arrhenius plot, taking only the total hole concentration at the defect site from the NEGF calculation.

The NMP defects show a strong temperature activation, in good agreement with experimental observation and in contrast to the SRH description. Also, the difference in temperature activation between line shapes calculated using the quantum mechanical formula of Eq. (4) and those calculated based on classical statistical physics Eq. (7) are compared. For the hydrogen bridge, this difference becomes vis-

ible only below 140 K. For the oxygen vacancy, the classical formula reproduces the quantum mechanical behavior over the complete temperature range investigated.

6 Conclusion

We report a detailed model to describe non-radiative multi phonon transitions in the context of reliability issues in semiconductor devices such as the bias temperature instability or random telegraph noise. Our approach combines a density functional theory for the defect and a non-equilibrium Green's function model for the device to obtain an accurate description of the real-world situation. The implementation of the non-radiative multi phonon transitions deviates from published implementations by employing numerically calculated line shapes instead of analytic expressions, which enables us to go beyond the usual assumption of linear electron-phonon coupling. This is very important, as our DFT-extracted potential energy surfaces show a strong difference between the spring constants of the neutral and the positive charge state of the defect c_i and c_f.

We have applied the method to hole capture in an MOS structure using two well-studied model defect structures, the hydrogen bridge and the oxygen vacancy in α-quartz. The calculations have been compared to experimental data obtained using the time-dependent defect spectroscopy method on small-area MOSFETs. The gate voltage dependence of the calculated capture time constants show good qualitative agreement with experiment. Also, the reported strong temperature activation can be explained by the NMP model. Line shapes calculated from classical statistical physics have been compared to their fully quantum mechanical counterparts. The classical approximation is shown to give a good approximation for the considered defects and the temperatures typically encountered during device operation.

Acknowledgement This work has received funding from the EC's FP7 grant agreement NMP.2010.2.5-1 (MORDRED).

References

1. Jeppson, K., Svensson, C.: J. Appl. Phys. **48**(5), 2004 (1977)
2. Schroder, D.K.: Microelectron. Reliab. **47**, 841 (2007)
3. Grasser, T., Kaczer, B., Goes, W., Aichinger, T., Hehenberger, P., Nelhiebel, M.: In: Proc. Intl. Rel. Phys. Symp., pp. 33–44 (2009)
4. Grasser, T., Kaczer, B., Gös, W., Reisinger, H., Aichinger, T., Hehenberger, P., Wagner, P.J., Schanovsky, F., Franco, J., Toledano-Luque, M., Nelhiebel, M.: IEEE Trans. Electron Devices **58**(11), 3652 (2011)
5. Kirton, M., Uren, M.: Appl. Phys. Lett. **48**, 1270 (1986)
6. Grasser, T., Reisinger, H., Wagner, P.J., Kaczer, B.: In: Proc. Intl. Rel. Phys. Symp., pp. 16–25 (2010)
7. Fleetwood, D., Xiong, H., Lu, Z.Y., Nicklaw, C., Felix, J., Schrimpf, R., Pantelides, S.: IEEE Trans. Nucl. Sci. **49**(6), 2674 (2002)
8. Kaczer, B., Grasser, T., Martin-Martinez, J., Simoen, E., Aoulaiche, M., Roussel, P., Groeseneken, G.: In: Proc. Intl. Rel. Phys. Symp., pp. 55–60 (2009)
9. Wagner, P., Aichinger, T., Grasser, T., Nelhiebel, M., Vandamme, L.: In: Proc. Intl. Conf. Noise Fluct., pp. 621–624 (2009)
10. Blöchl, P.E., Stathis, J.H.: Phys. Rev. Lett. **83**(2), 372 (1999)
11. Blöchl, P.E.: Phys. Rev. B **62**(10), 6158 (2000)
12. Huang, K., Rhys, A.: Proc. R. Soc. A **204**, 406 (1950)
13. Henry, C.H., Lang, D.V.: Phys. Rev. B **15**(15), 989 (1977)
14. Makram-Ebeid, S., Lannoo, M.: Phys. Rev. B **25**(10), 6406 (1982)
15. Palma, A., Godoy, A., Jemènez-Tejada, J.A., Carceller, J.E., Lòpez-Villanueva, J.A.: Phys. Rev. B **56**(15), 9565 (1997)
16. Garetto, D., Randiamihaja, Y.M., Rideau, D., Dornel, E., Clark, W.F., Schmid, A., Huard, V., Jaouen, H., Leblebici, Y.: In: Proc. Intl. Worksh. Comput. Electron., pp. 327–330 (2010)
17. Zheng, J.H., Tan, H.S., Ng, S.C.: J. Phys., Condens. Matter **6**, 1695 (1994)
18. Grasser, T., Reisinger, H., Goes, W., Aichinger, T., Hehenberger, P., Wagner, P., Nelhiebel, M., Franco, J., Kaczer, B.: In: Proc. Intl. Electron Devices Meeting, pp. 729–732 (2009)
19. Reisinger, H., Grasser, T., Schlünder, C., Gustin, W.: In: Proc. Intl. Rel. Phys. Symp., pp. 7–15 (2010)
20. Grasser, T., Reisinger, H., Wagner, P., Kaczer, B.: Phys. Rev. B **82**, 245318 (2010)
21. Schanovsky, F., Goes, W., Grasser, T.: J. Comput. Electron. **9**, 135 (2010)
22. Schanovsky, F.: In: Proc. Intl. Worksh. Comput. Electron., pp. 163–166 (2010)
23. Schanovsky, F., Goes, W., Grasser, T.: J. Vac. Sci. Technol. B **29**, 01A201 (2011)
24. Schanovsky, F., Baumgartner, O., Grasser, T.: In: Proc. Simu. Semicond. Proc. Dev., pp. 15–18 (2011)
25. Schenk, A.: J. Appl. Phys. **71**, 3339 (1992)
26. Zapol, B.: Chem. Phys. Lett. **93**(6), 549 (1982)
27. Schmidt, P.P.: Mol. Phys. **108**, 1513 (2010)
28. Abakumov, V., Perel, V., Yassievich, I.: Nonradiative Recombination in Semiconductors. North-Holland, Amsterdam (1991)
29. Grasser, T.: Microelectron. Reliab. **52**(1), 39 (2011). doi:10.1016/j.microrel.2011.09.002
30. Baumgartner, O., Karner, M., Kosina, H.: In: Proc. Simu. Semicond. Proc. Dev., pp. 353–356 (2008). doi:10.1109/SISPAD.2008.4648310
31. Kresse, G., Furthmüller, J.: Phys. Rev. B **54**(11), 11169 (1996)
32. Kresse, G., Joubert, D.: Phys. Rev. B **59**, 1758 (1999)
33. Rudra, J.K., Fowler, W.B.: Phys. Rev. B **35**(15), 8223 (1987)
34. Mysovsky, A.S., Sushko, P.V., Mukhopadhyay, S., Edwards, A.H., Shluger, A.L.: Phys. Rev. B **69**(8), 085202 (2004)
35. Drabold, D.A., Estreicher, S.K. (eds.): Theory of Defects in Semiconductors. Springer, Berlin (2010)
36. Karner, M., Gehring, A., Holzer, S., Pourfath, M., Wagner, M., Goes, W., Vasicek, M., Baumgartner, O., Kernstock, C., Schnass, K., Zeiler, G., Grasser, T., Kosina, H., Selberherr, S.: J. Comput. Electron. **6**, 179 (2007). doi:10.1007/s10825-006-0077-7
37. Shockley, W., Read, W.T.: Phys. Rev. **87**, 835 (1952)
38. Schenk, A.: Solid-State Electron. **35**, 1585 (1992)